

<sup>1</sup> High-level cognition during story listening is reflected in  
<sup>2</sup> high-order dynamic correlations in neural activity patterns

<sup>3</sup> Lucy L. W. Owen<sup>1</sup>, Thomas H. Chang<sup>1,2</sup>, and Jeremy R. Manning<sup>1,†</sup>

<sup>1</sup>Department of Psychological and Brain Sciences,  
Dartmouth College, Hanover, NH

<sup>2</sup>Amazon.com, Seattle, WA

<sup>†</sup>Address correspondence to jeremy.r.manning@dartmouth.edu

<sup>4</sup> September 5, 2019

<sup>5</sup> **Abstract**

Our thoughts arise from coordinated patterns of interactions between brain structures that change with our ongoing experiences. High-order dynamic correlations in neural activity patterns reflect different subgraphs of the brain’s connectome that display homologous lower-level dynamic correlations. We tested the hypothesis that high-level cognition is supported by high-order dynamic correlations in brain activity patterns. We developed an approach to estimating high-order dynamic correlations in timeseries data, and we applied the approach to neuroimaging data collected as human participants either listened to a ten-minute story, listened to a temporally scrambled version of the story, or underwent a resting state scan. We trained across-participants pattern classifiers to decode (in held-out data) when in the session each neural activity snapshot was collected. We found that classifiers trained to decode from high-order dynamic correlations yielded the best performance on data collected as participants listened to the (unscrambled) story. By contrast, classifiers trained to decode data from scrambled versions of the story or during the resting state scan yielded the best performance when they were trained using first-order dynamic correlations or non-correlational activity patterns. We suggest that as our thoughts become more complex, they are supported by higher-order patterns of dynamic network interactions throughout the brain.

<sup>20</sup> **Introduction**

A central goal in cognitive neuroscience is to elucidate the *neural code*: the mapping between (a) mental states or cognitive representations and (b) neural activity patterns. One means of testing models of the neural code is to ask how accurately that model is able to “translate” neural activity patterns into known (or hypothesized) mental states or cognitive representations (e.g., Haxby et al., 2001; Huth et al., 2016, 2012; Kamitani & Tong, 2005; Mitchell et al., 2008; Nishimoto et al., 2011; Norman et al., 2006; Pereira et al., 2018; Tong & Pratte, 2012). Training decoding models on different types of neural features (Fig. 1a) can also help to elucidate which specific aspects of neural activity patterns are informative about cognition—and, by extension, which types of neural activity patterns might comprise the neural code. For example, prior work has used region of interest analyses to estimate the anatomical locations of specific neural representations (e.g., Etzel et al., 2009), or to compare the relative contributions to the neural code of

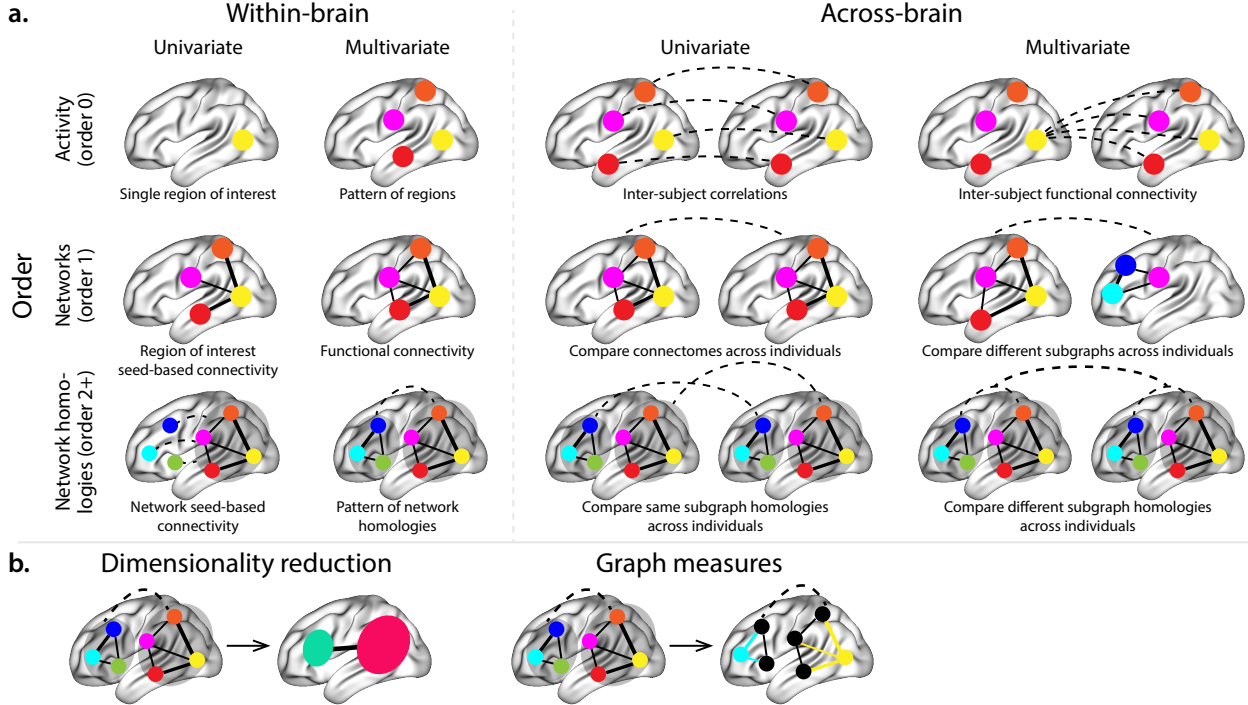


**Figure 1: Neural patterns. a. A space of neural analyses** Within-brain analyses are carried out within a single brain, whereas across-brain analyses compare neural patterns across two or more individuals' brains. Univariate analyses characterize the activities of individual units (e.g., nodes, small networks, hierarchies of networks, etc.), whereas multivariate analyses characterize the patterns of activities across units. Order 0 patterns involve individual nodes; order 1 patterns involve node-node interactions; order 2 (and higher) patterns relate to interactions between homologous networks. Each of these patterns may be static (e.g., averaging over time) or dynamic. **b. Summarizing neural patterns.** To efficiently compute with complex neural patterns, it can be useful to characterize the patterns using summary measures. Dimensionality reduction algorithms project the patterns onto lower-dimensional spaces whose dimensions reflect weighted combinations of the dimensions in the original space. Graph measures characterize each unit's participation in its associated network.

31 multivariate activity patterns versus patterns of dynamic correlations between neural activity patterns (e.g.,  
 32 Fong et al., 2019; Manning et al., 2018). An emerging theme in this literature is that cognition is mediated by  
 33 dynamic interactions between brain structures (Bassett et al., 2006; Demertzi et al., 2019; Lurie et al., 2018;  
 34 Mack et al., 2017; Preti et al., 2017; Solomon et al., 2019; Sporns & Honey, 2006; Turk-Browne, 2013; Zou et  
 35 al., 2019).

36 Studies of the neural code to date have primarily focused on univariate or multivariate neural pat-  
 37 terns (for review see Norman et al., 2006), or (more recently) on patterns of dynamic first-order correla-  
 38 tions (i.e., interactions between pairs of brain structures; Demertzi et al., 2019; Fong et al., 2019; Lurie et  
 39 al., 2018; Manning et al., 2018; Preti et al., 2017; Zou et al., 2019). We wondered what the future of this  
 40 line of work might hold. For example, is the neural code mediated by higher-order interactions between

41 brain structures (e.g., see Reimann et al., 2017)? Second-order correlations reflect *homologous* patterns of  
42 correlation. In other words, if the dynamic patterns of correlations between two regions, *A* and *B*, are similar  
43 to those between two other regions, *C* and *D*, this would be reflected in the second-order correlations be-  
44 tween (*A*-*B*) and (*C*-*D*). In this way, second-order correlations identify similarities and differences between  
45 subgraphs of the brain’s connectome. Analogously, third-order correlations reflect homologies between  
46 second-order correlations— i.e., homologous patterns of homologous interactions between brain regions.  
47 More generally, higher-order correlations reflect homologies between patterns of lower-order correlations.  
48 We can then ask: which “orders” of interaction are most reflective of high-level cognitive processes?

49 Another central question pertains to the extent to which the neural code is carried by activity patterns  
50 that directly reflect ongoing cognition (e.g., following Haxby et al., 2001; Norman et al., 2006), versus the  
51 dynamic properties of the network structure itself, independent of specific activity patterns in any given  
52 set of regions (e.g., following Bassett et al., 2006). For example, graph measures such as centrality and  
53 degree (Bullmore & Sporns, 2009) may be used to estimate how a given brain structure is “communicating”  
54 with other structures, independently of the specific neural representations carried by those structures.  
55 If one considers a brain region’s position in the network (e.g., its eigenvector centrality) as a dynamic  
56 property, one can compare how the positions of different regions are correlated, and/or how those patterns  
57 of correlations change over time. We can also compute higher-order patterns in these correlations to  
58 characterize homologous subgraphs in the connectome that display similar changes in their constituent  
59 brain structures’ interactions with the rest of the brain.

60 To gain insights into the above aspects of the neural code, we developed a computational framework  
61 for estimating dynamic high-order correlations in timeseries data. This framework provides an important  
62 advance, in that it enables us to examine patterns in higher-order correlations that are computationally  
63 intractable to estimate via conventional methods. Given a multivariate timeseries, our framework provides  
64 timepoint-by-timepoint estimates of the first-order correlations, second-order correlations, and so on. Our  
65 approach combines a kernel-based method for computing dynamic correlations in timeseries data with a di-  
66 mensionality reduction step (Fig. 1b) that projects the resulting dynamic correlations into a low-dimensional  
67 space. We explored two dimensionality reduction approaches: principle components analysis (PCA; Pear-  
68 son, 1901), which preserves an approximately invertible transformation back to the original data (e.g., this  
69 follows related approaches taken by Gonzalez-Castillo et al., 2019; McIntosh & Jirsa, 2019; Toker & Som-  
70 mer, 2019); and a second non-invertible algorithm that explored patterns in eigenvector centrality (Landau,  
71 1895). This latter approach characterizes correlations between each feature dimension’s relative *position* in  
72 the network in favor of the specific activity histories of different features (also see Betzel et al., 2019; Reimann  
73 et al., 2017; Sizemore et al., 2018).

74 We validated our approach using synthetic data where the underlying correlations were known. We  
75 then applied our framework to a neuroimaging dataset collected as participants listened to either an audio  
76 recording of a ten-minute story or a temporally scrambled version of the story, or underwent a resting  
77 state scan (Simony et al., 2016). We used a subset of the data to train across-participant classifiers to  
78 decode listening times using a blend of neural features (comprising neural activity patterns, as well as  
79 different orders of dynamic correlations between those patterns that were inferred using our computational  
80 framework). We found that both the PCA-based and eigenvector centrality-based approaches yielded neural  
81 patterns that could be used to decode accurately (i.e., well above chance). Both approaches also yielded  
82 the best decoding accuracy for data collected during (intact) story listening when high-order (PCA: second-  
83 order; eigenvector centrality: fourth-order) dynamic correlation patterns were included as features. When  
84 we trained classifiers on the scrambled stories or resting state data, only lower-order dynamic patterns were  
85 informative to the decoders. Taken together, our results indicate that high-level cognition is supported by  
86 high-order dynamic patterns of communication between brain structures.

## 87 Methods

88 Our general approach to efficiently estimating high-order dynamic correlations comprises four general  
89 steps (Fig. 2). First, we derive a kernel-based approach to computing dynamic pairwise correlations in  
90 a  $T$  (timepoints) by  $K$  (features) multivariate timeseries,  $\mathbf{X}_0$ . This yields a  $T$  by  $O(K^2)$  matrix of dynamic  
91 correlations,  $\mathbf{Y}_1$ , where each row comprises the upper triangle and diagonal of the correlation matrix at  
92 a single timepoint, reshaped into a row vector (this reshaped vector is  $(\frac{K^2-K}{2} + K)$ -dimensional). Second,  
93 we apply a dimensionality reduction step to project the matrix of dynamic correlations back onto a  $K$ -  
94 dimensional space. This yields a  $T$  by  $K$  matrix,  $\mathbf{X}_1$ , that reflects an approximation of the dynamic correlations  
95 reflected in the original data. Third, we use repeated applications of the kernel-based dynamic correlation  
96 step to  $\mathbf{X}_n$  and the dimensionality reduction step to the resulting  $\mathbf{Y}_{n+1}$  to estimate high-order dynamic  
97 correlations. Each application of these steps to a  $T$  by  $K$  time series  $\mathbf{X}_n$  yields a  $T$  by  $K$  matrix,  $\mathbf{X}_{n+1}$ , that  
98 reflects the dynamic correlations between the columns of  $\mathbf{X}_n$ . In this way, we refer to  $n$  as the *order* of the  
99 timeseries, where  $\mathbf{X}_0$  (order 0) denotes the original data and  $\mathbf{X}_n$  denotes (approximated)  $n^{\text{th}}$ -order dynamic  
100 correlations between the columns of  $\mathbf{X}_0$ . Finally, we use a cross-validation-based decoding approach to  
101 evaluate how well information contained in a given order (or weighted mixture of orders) may be used  
102 to decode relevant cognitive states. If including a given  $\mathbf{X}_n$  in the feature set yields higher classification  
103 accuracy on held-out data, we interpret this as evidence that the given cognitive states are reflected in  
104 patterns of  $n^{\text{th}}$ -order correlations. All of the code used to produce the figures and results in this manuscript,

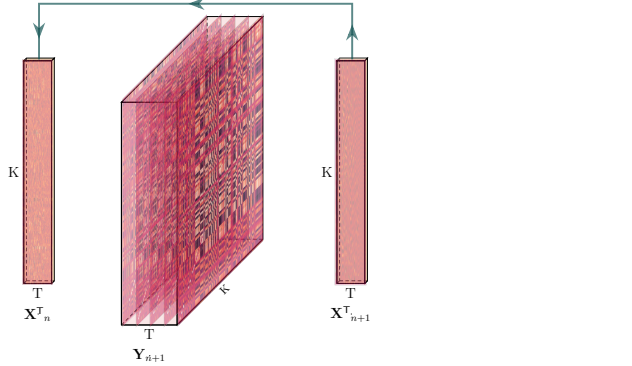


Figure 2: **Estimating dynamic high-order correlations.** Given a  $T$  by  $K$  matrix of multivariate timeseries data,  $\mathbf{X}_n$  (where  $n \in \mathbb{N}, n \geq 0$ ), we use Equation 4 to compute a timeseries of  $K$  by  $K$  correlation matrices,  $\mathbf{Y}_{n+1}$ . We then approximate  $\mathbf{Y}_{n+1}$  with the  $T$  by  $K$  matrix  $\mathbf{X}_{n+1}$ . This process may be repeated to scalably estimate iteratively higher-order correlations in the data. Note that the transposes of  $\mathbf{X}_n$  and  $\mathbf{X}_{n+1}$  are displayed in the figure for compactness.

105 along with links to the corresponding datasets, may be found at [github.com/ContextLab/timecorr-paper](https://github.com/ContextLab/timecorr-paper). In  
 106 addition, we have released a Python toolbox for computing dynamic high-order correlations in timeseries  
 107 data; our toolbox may be found at [timecorr.readthedocs.io](https://timecorr.readthedocs.io). **JRM NOTE: CHECK LINK**

## 108 Kernel-based approach for computing dynamic correlations

Given a  $T$  by  $K$  matrix of observations,  $\mathbf{X}$ , we can compute the (static) Pearson's correlation between any pair of columns,  $\mathbf{X}(\cdot, i)$  and  $\mathbf{X}(\cdot, j)$  using (Pearson, 1901):

$$\text{corr}(\mathbf{X}(\cdot, i), \mathbf{X}(\cdot, j)) = \frac{\sum_{t=1}^T (\mathbf{X}(t, i) - \bar{\mathbf{X}}(\cdot, i))(\mathbf{X}(t, j) - \bar{\mathbf{X}}(\cdot, j))}{\sqrt{\sum_{t=1}^T \sigma_{\mathbf{X}(\cdot, i)}^2 \sigma_{\mathbf{X}(\cdot, j)}^2}}, \text{ where} \quad (1)$$

$$\bar{\mathbf{X}}(\cdot, k) = \frac{1}{T} \sum_{t=1}^T \mathbf{X}(t, k), \text{ and} \quad (2)$$

$$\sigma_{\mathbf{X}(\cdot, k)}^2 = \frac{1}{T} \sum_{t=1}^T (\mathbf{X}(t, k) - \bar{\mathbf{X}}(\cdot, k))^2 \quad (3)$$

109 We can generalize this formula to compute time-varying correlations by incorporating a *kernel function* that  
 110 takes a time  $t$  as input, and returns how much the observed data at each timepoint  $\tau \in [-\infty, \infty]$  contributes  
 111 to the estimated instantaneous correlation at time  $t$  (Fig. 3; also see Allen et al., 2012, for a similar approach).

112

Given a kernel function  $\kappa_t(\cdot)$  for timepoint  $t$ , evaluated at timepoints  $\tau \in [1, \dots, T]$ , we can update the

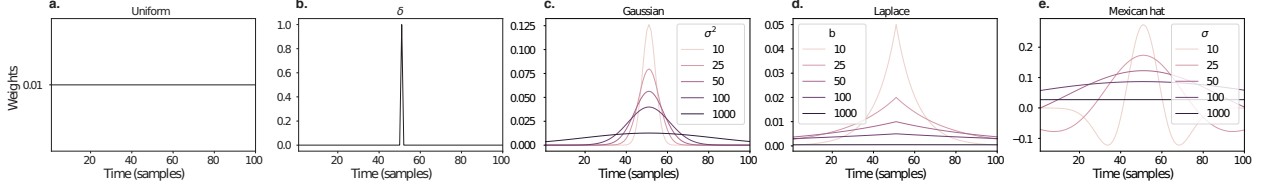


**Figure 3: Examples of kernel functions.** Each panel displays per-timepoint weights for a kernel centered at  $t = 50$ , evaluated at 100 timepoints ( $\tau \in [1, \dots, 100]$ ). **a. Uniform kernel.** The weights are timepoint-invariant; observations at all timepoints are weighted equally, and do not change as a function of  $\tau$ . This is a special case kernel function that reduces dynamic correlations to static correlations. **b. Dirac  $\delta$  kernel.** Only the observation at timepoint  $t$  is given a non-zero weight (of 1). **c. Gaussian kernels.** Each kernel's weights fall off in time according to a Gaussian probability density function centered on time  $t$ . Weights derived using several different example width parameters ( $\sigma^2$ ) are displayed. **d. Laplace kernels.** Each kernel's weights fall off in time according to a Laplace probability density function centered on time  $t$ . Weights derived using several different example width parameters ( $b$ ) are displayed. **e. Mexican hat (Ricker wavelet) kernels.** Each kernel's weights fall off in time according to a Ricker wavelet centered on time  $t$ . This function highlights the *contrasts* between local versus surrounding activity patterns in estimating dynamic correlations. Weights derived using several different example width parameters ( $\sigma$ ) are displayed.

static correlation formula in Equation 2 to estimate the *instantaneous correlation* at timepoint  $t$ :

$$\text{timecorr}_{\kappa_t}(\mathbf{X}(\cdot, i), \mathbf{X}(\cdot, j)) = \frac{\sum_{\tau=1}^T (\mathbf{X}(\tau, i) - \tilde{\mathbf{X}}_{\kappa_t}(\cdot, i))(\mathbf{X}(\tau, j) - \tilde{\mathbf{X}}_{\kappa_t}(\cdot, j))}{\sqrt{\sum_{\tau=1}^T \tilde{\sigma}_{\kappa_t}^2(\mathbf{X}(\tau, i)) \tilde{\sigma}_{\kappa_t}^2(\mathbf{X}(\tau, j))}}, \text{ where} \quad (4)$$

$$\tilde{\mathbf{X}}_{\kappa_t}(t) = \sum_{\tau=1}^T \kappa_t(\tau) \mathbf{X}(\tau, k), \quad (5)$$

$$\tilde{\sigma}_{\kappa_t}^2(\mathbf{X}(\cdot, k)) = \sum_{\tau=1}^T (\mathbf{X}(\tau, k) - \tilde{\mathbf{X}}_{\kappa_t}(t, k))^2. \quad (6)$$

113 Here  $\text{timecorr}_{\kappa_t}(\mathbf{X}(\cdot, i), \mathbf{X}(\cdot, j))$  reflects the correlation at time  $t$  between columns  $i$  and  $j$  of  $\mathbf{X}$ , estimated using  
 114 the kernel  $\kappa_t$ . We evaluate Equation 4 in turn each pair of columns in  $\mathbf{X}$  and for kernels centered on each  
 115 timepoint in the timeseries, respectively, to obtain a  $T$  by  $K$  by  $K$  timeseries of dynamic correlations,  $\mathbf{Y}$ . For  
 116 convenience, we then reshape the upper triangles and diagonals of each timepoint's correlation matrix into  
 117 a row vector to obtain an equivalent  $T$  by  $\left(\frac{K^2-K}{2} + K\right)$  matrix.

#### 118 **Dynamic inter-subject functional connectivity (DISFC)**

Equation 4 provides a means of taking a single observation matrix,  $\mathbf{X}_n$  and estimating the dynamic correlations from moment to moment,  $\mathbf{Y}_{n+1}$ . Suppose that one has access to a set of multiple observation matrices that reflect the same phenomenon. For example, one might collect neuroimaging data from several experimental participants, as each participant performs the same task (or sequence of tasks). Let  $\mathbf{X}_n^1, \mathbf{X}_n^2, \dots, \mathbf{X}_n^P$  reflect the  $T$  by  $K$  observation matrices ( $n = 0$ ) or reduced correlation matrices ( $n > 0$ ) for each of  $P$

participants in an experiment. We can use *inter-subject functional connectivity* (ISFC; Simony et al., 2016) to compute the stimulus-driven correlations reflected in the multi-participant dataset at a given timepoint  $t$  using:

$$\bar{\mathbf{C}}(t) = M \left( R \left( \frac{1}{2P} \sum_{p=1}^P Z(Y_n^p(t))^T + Z(Y_n^p(t)) \right) \right), \quad (7)$$

where  $M$  extracts and vectorizes the diagonal and upper triangle of a symmetric matrix,  $Z$  is the Fisher z-transformation (Zar, 2010):

$$Z(r) = \frac{\log(1+r) - \log(1-r)}{2} \quad (8)$$

$R$  is the inverse of  $Z$ :

$$R(z) = \frac{\exp(2z-1)}{\exp(2z+1)}, \quad (9)$$

and  $\mathbf{Y}_n^p(t)$  denotes the correlation matrix at timepoint  $t$  (Eqn. 4) between each column of  $\mathbf{X}_n^p$  and each column of the average  $\mathbf{X}_n$  from all *other* participants,  $\bar{\mathbf{X}}_n^{\setminus p}$ :

$$\bar{\mathbf{X}}_n^{\setminus p} = R \left( \frac{1}{P-1} \sum_{q \in \setminus p} Z(\mathbf{x}_n^q) \right), \quad (10)$$

119 where  $\setminus p$  denotes the set of all participants other than participant  $p$ . In this way, the  $T$  by  $(\frac{K^2-K}{2} + K)$  DISFC  
120 matrix  $\bar{\mathbf{C}}$  provides a time-varying extension of the ISFC approach developed by Simony et al. (2016).

## 121 Low-dimensional representations of dynamic correlations

122 Given a  $T$  by  $(\frac{K^2-K}{2} + K)$  matrix of dynamic correlations,  $\mathbf{Y}_n$ , we propose two general approaches to computing  
123 a  $T$  by  $K$  low-dimensional representation of those correlations,  $\mathbf{X}_n$ . The first approach uses dimensionality  
124 reduction algorithms to project  $\mathbf{Y}_n$  onto a  $K$ -dimensional space. The second approach uses graph measures  
125 to characterize the relative positions of each feature ( $k \in [1, \dots, K]$ ) in the network defined by the correlation  
126 matrix at each timepoint.

## 127 Dimensionality reduction-based approaches to computing $\mathbf{X}_n$

128 The modern toolkit of dimensionality reduction algorithms include Principal Components Analysis (PCA;  
129 Pearson, 1901), Probabilistic PCA (PPCA; Tipping & Bishop, 1999), Exploratory Factor Analysis (EFA;

130 Spearman, 1904), Independent Components Analysis (ICA; Comon et al., 1991; Jutten & Herault, 1991),  
131  $t$ -Stochastic Neighbor Embedding ( $t$ -SNE; van der Maaten & Hinton, 2008), Uniform Manifold Approximation and Projection (UMAP; McInnes & Healy, 2018), non-negative matrix factorization (NMF; Lee &  
132 Seung, 1999), Topographic Factor Analysis (TFA; Manning et al., 2014), Hierarchical Topographic Factor  
133 analysis (HTFA; Manning et al., 2018), Topographic Latent Source Analysis (TLSA; Gershman et al., 2011),  
134 Dictionary learning (J. Mairal et al., 2009; J. B. Mairal et al., 2009), deep auto-encoders (Hinton & Salakhutdinov, 2006), among others. While complete characterizations of each of these algorithms is beyond the scope  
135 of the present manuscript, the general intuition driving these approaches is to compute the  $T$  by  $M$  matrix,  
136  $\mathbf{X}$ , that is closest to the original  $T$  by  $N$  matrix,  $\mathbf{Y}$ , where (typically)  $M \ll N$ . The different approaches place  
137 different constraints on what properties  $\mathbf{X}$  must satisfy and which aspects of the data are compared (and  
138 how) in order to characterize how well  $\mathbf{X}$  approximates  $\mathbf{Y}$ .

141 Applying dimensionality reduction algorithms to  $\mathbf{Y}$  yields an  $\mathbf{X}$  whose columns reflect weighted combinations  
142 (or nonlinear transformations) of the original columns of  $\mathbf{Y}$ . This has two main consequences. First,  
143 with each repeated dimensionality reduction, the resulting  $\mathbf{X}_n$  has lower and lower fidelity (with respect to  
144 what the “true”  $\mathbf{Y}_n$  might have looked like without using dimensionality reduction to maintain scalability).  
145 In other words, computing  $\mathbf{X}_n$  is a lossy operation. Second, whereas each columns of  $\mathbf{Y}_n$  may always be  
146 mapped directly onto specific pairs of columns of  $\mathbf{Y}_{n-1}$ , the columns of  $\mathbf{X}_n$  reflect weighted combinations  
147 and/or nonlinear transformations of the columns of  $\mathbf{Y}_n$ . Many dimensionality reduction algorithms are  
148 invertible (or approximately invertible). However, attempting to map a given  $\mathbf{X}_n$  back onto the original  
149 feature space of  $\mathbf{Y}_0$  will usually require  $O(TK^{2n})$  space and therefore quickly becomes intractable as  $n$  or  $K$   
150 grow large.

### 151 **Graph measure approaches to computing $\mathbf{X}_n$**

152 The above dimensionality reduction approaches to approximating a given  $\mathbf{Y}_n$  with a lower-dimensional  
153  $\mathbf{X}_n$  preserve a (potentially recombined and transformed) mapping back to the original data in  $\mathbf{X}_0$ . We also  
154 explore graph measures that instead characterize each feature’s relative *position* in the broader network of  
155 interactions and connections. To illustrate the distinction between the two general approaches we explore,  
156 suppose a network comprises nodes  $A$ ,  $B$ , and  $C$ . If  $A$  and  $B$  exhibit uncorrelated activity patterns, the  
157 functional connection (correlation) between them will be (by definition) close to 0. However, if  $A$  and  $B$   
158 each interact with  $C$  in similar ways, we might attempt to capture those similarities using a measure that  
159 reflects how  $A$  and  $B$  interact with *other* members of the network.

160 In general, graph measures take as input a matrix of interactions (e.g., using the above notation, a  $K$

161 by  $K$  correlation matrix or binarized correlation matrix reconstituted from a single timepoint's row of  $\mathbf{Y}$ )  
162 and return as output a set of  $K$  measures describing how each node (feature) sits within that correlation  
163 matrix with respect to the rest of the population. Widely used measures include betweenness centrality (the  
164 proportion of shortest paths between each pair of nodes in the population that involves the given node  
165 in question; e.g., Barthélemy, 2004; Freeman, 1977; Geisberger et al., 2008; Newman, 2005; Opsahl et al.,  
166 2010); diversity and dissimilarity (characterizations of how differently connected a given node is from others  
167 in the population; e.g., Lin, 2009; Rao, 1982; Ricotta & Szeidl, 2006); Eigenvector centrality and pagerank  
168 centrality (measures of how influential a given node is within the broader network; e.g., Bonacich, 2007;  
169 Halu et al., 2013; Lohmann et al., 2010; Newman, 2008); transfer entropy and flow coefficients (a measure  
170 of how much information is flowing from a given node to other nodes in the network; e.g., Honey et  
171 al., 2007; Schreiber, 2000);  $k$ -coreness centrality (a measure of the connectivity of a node within its local  
172 sub-graph; e.g., Alvarez-Hamelin et al., 2005; Christakis & Fowler, 2010); within-module degree (a measure  
173 of how many connections a node has to its close neighbors in the network; e.g., Rubinov & Sporns, 2010);  
174 participation coefficient (a measure of the diversity of a node's connections to different sub-graphs in the  
175 network; e.g., Rubinov & Sporns, 2010); and sub-graph centrality (a measure of a node's participation in all  
176 of the network's sub-graphs; e.g., Estrada & Rodríguez-Velázquez, 2005); among others.

177 For a given graph measure,  $\eta : \mathbb{R}^{K \times K} \rightarrow \mathbb{R}^K$ , we can use  $\eta$  to transform each row of  $\mathbf{Y}_n$  in a way that  
178 characterizes the corresponding graph properties of each column. This results in a new  $T$  by  $K$  matrix,  $\mathbf{X}_n$ ,  
179 that reflects how the features reflected in the columns of  $\mathbf{Y}_n$  participate in the network during each timepoint  
180 (row).

## 181 Dynamic higher-order correlations

182 Because  $\mathbf{X}_n$  has the same shape as the original data  $\mathbf{X}_0$ , approximating  $\mathbf{Y}_n$  with a lower-dimensional  $\mathbf{X}_n$   
183 enables us to estimate high-order dynamic correlations in a scalable way. Given a  $T$  by  $K$  input matrix, the  
184 output of Equation 4 requires  $O(TK^2)$  space to store. Repeated applications of Equation 4 (i.e., computing  
185 dynamic correlations between the columns of the outputted dynamic correlation matrix) each require  
186 exponentially more space; in general the  $n^{\text{th}}$ -order dynamic correlations of a  $T$  by  $K$  timeseries occupies  
187  $O(TK^{2n})$  space. However, when we approximate or summarize the output of Equation 4 with a  $T$  by  $K$  matrix  
188 (as described above), it becomes feasible to compute even very high-order correlations in high-dimensional  
189 data. Specifically, approximating the  $n^{\text{th}}$ -order dynamic correlations of a  $T$  by  $K$  timeseries requires only  
190  $O(TK^2)$  additional space— the same as would be required to compute first-order dynamic correlations. In  
191 other words, the space required to store  $n + 1$  multivariate timeseries reflecting up to  $n^{\text{th}}$  order correlations

192 in the original data scales linearly with  $n$  using our approach (Fig. 2).

193 **Data**

194 We examined two types of data: synthetic data and human functional neuroimaging data. We constructed  
195 and leveraged the synthetic data to evaluate our general approach (for a related validation approach, see  
196 Thompson et al., 2018). Specifically, we tested how well Equation 4 could be used to recover known dynamic  
197 correlations using different choices of kernel ( $\kappa$ ; Fig. 3), for each of several synthetic datasets that exhibited  
198 different temporal properties. We applied our approach to a functional neuroimaging dataset to test the  
199 hypothesis that ongoing cognitive processing is reflected in high-order dynamic correlations. We used an  
200 across-participant classification test to estimate whether dynamic correlations of different orders contain  
201 information about which timepoint in a story participants were listening to.

202 **Synthetic data**

203 We constructed a total of 40 different multivariate timeseries, collectively reflecting a total of 4 qualitatively  
204 different patterns of dynamic correlations (i.e., 10 datasets reflecting each type of dynamic pattern). Each  
205 timeseries comprised 50 features (dimensions) that varied over 300 timepoints. The observations at each  
206 timepoint were drawn from a zero-mean multivariate Gaussian distribution with a covariance matrix  
207 defined for each timepoint as described below. We drew the observations at each timepoint independently  
208 from the draws at all other timepoints; in other words, for each observation  $s_t \sim \mathcal{N}(\mathbf{0}, \Sigma_t)$  at timepoint  $t$ ,  
209  $p(s_t) = p(s_t | s_{\setminus t})$ .

**Constant.** We generated data with stable underlying correlations to evaluate how Equation 4 characterized correlation “dynamics” when the ground truth correlations were static. We constructed 10 multivariate timeseries whose observations were each drawn from a single (stable) Gaussian distribution. For each dataset (indexed by  $m$ ), we constructed a random covariance matrix,  $\Sigma_m$ :

$$\mathbf{C}(i, j) \sim \mathcal{N}(0, 1) \quad (11)$$

$$\Sigma_m = \mathbf{C}\mathbf{C}^\top, \text{ where} \quad (12)$$

210  $i, j \in [1, 2, \dots, 50]$ . In other words, all of the observations (for each of the 300 timepoints) within each dataset  
211 were drawn from a multivariate Gaussian distribution with the same covariance matrix, and the 10 datasets  
212 each used a different covariance matrix.

213 **Random.** We generated a second set of 10 synthetic datasets whose observations at each timepoint were  
214 drawn from a Gaussian distribution with a new randomly constructed (using Eqn. 12) covariance matrix.  
215 Because each timepoint’s covariance matrix was drawn independently from the covariance matrices for all  
216 other timepoints, these datasets provided a test of reconstruction accuracy in the absence of any meaningful  
217 underlying temporal structure in the dynamic correlations underlying the data.

**Ramping.** We generated a third set of 10 synthetic datasets whose underlying correlations changed gradually over time. For each dataset, we constructed two *anchor* correlation matrices using Equation 12,  $\Sigma_{\text{start}}$  and  $\Sigma_{\text{end}}$ . For each of the 300 timepoints in each dataset, we drew the observations from a multivariate Gaussian distribution whose covariance matrix at each timepoint  $t \in [0, \dots, 299]$  was given by

$$\Sigma_t = \left(1 - \frac{t}{299}\right)\Sigma_{\text{start}} + \frac{t}{299}\Sigma_{\text{end}}. \quad (13)$$

218 The gradually changing correlations underlying these datasets allow us to evaluate the recovery of dynamic  
219 correlations when each timepoint’s correlation matrix is unique (as in the random datasets), but where the  
220 correlation dynamics are structured.

221 **Event.** We generated a fourth set of 10 synthetic datasets whose underlying correlation matrices exhibited  
222 prolonged intervals of stability, interspersed with abrupt changes. For each dataset, we used Equation 12  
223 to generate 5 random covariance matrices. We constructed a timeseries where each set of 60 consecutive  
224 samples was drawn from a Gaussian with the same covariance matrix. These datasets were intended to  
225 simulate a system that undergoes occasional abrupt state changes.

## 226 Functional neuroimaging data collected during story listening

227 We examined an fMRI dataset collected by Simony et al. (2016) that the authors have made publicly available  
228 at [arks.princeton.edu/ark:/88435/dsp015d86p269k](http://arks.princeton.edu/ark:/88435/dsp015d86p269k). The dataset comprises neuroimaging data collected as  
229 participants listened to an audio recording of a story (intact condition; 36 participants), listened to time  
230 scrambled recordings of the same story (17 participants in the paragraph-scrambled condition listened to  
231 the paragraphs in a randomized order and 36 in the word-scrambled condition listened to the words in a  
232 randomized order), or lay resting with their eyes open in the scanner (rest condition; 36 participants). Full  
233 neuroimaging details may be found in the original paper for which the data were collected (Simony et al.,  
234 2016).

235 **Hierarchical topographic factor analysis (HTFA).** Following our prior related work, we used HTFA (Manning et al., 2018) to derive a compact representation of the neuroimaging data. In brief, this approach approximates the timeseries of voxel activations (44,415 voxels) using a much smaller number of radial basis function (RBF) nodes (in this case, 700 nodes, as determined by an optimization procedure described by Manning et al., 2018). This provides a convenient representation for examining full-brain network dynamics. All of the analyses we carried out on the neuroimaging dataset were performed in this lower-dimensional space. In other words, each participant’s data matrix,  $\mathbf{X}_0$ , was a number-of-timepoints by 700 matrix of HTFA-derived factor weights (where the row and column labels were matched across participants). Code for carrying out HTFA on fMRI data may be found as part of the BrainIAK toolbox (Capota et al., 2017), which may be downloaded at [brainiak.org](http://brainiak.org).

## 245 Temporal decoding

246 We sought to identify neural patterns that reflected participants’ ongoing cognitive processing of incoming  
247 stimulus information. As reviewed by Simony et al. (2016), one way of homing in on these stimulus-  
248 driven neural patterns is to compare activity patterns across individuals (e.g., using ISFC analyses). In  
249 particular, neural patterns will be similar across individuals to the extent that the neural patterns under  
250 consideration are stimulus-driven, and to the extent that the corresponding cognitive representations are  
251 reflected in similar spatial patterns across people. Following this logic, we used an across-participants  
252 temporal decoding test developed by Manning et al. (2018) to assess the degree to which different neural  
253 patterns reflected ongoing stimulus-driven cognitive processing across people. The approach entails using  
254 a subset of the data to train a classifier to decode stimulus timepoints (i.e., moment in the story participants  
255 listened to) from neural patterns. We use decoding (forward inference) accuracy on held-out data, from held-  
256 out participants, as a proxy for the extent to which the inputted neural patterns reflected stimulus-driven  
257 cognitive processing in a similar way across individuals.

## 258 Forward inference and decoding accuracy

259 We used an across-participants correlation-based classifier to decode which stimulus timepoint matched  
260 each timepoint’s neural pattern. We first divided the participants into two groups: a template group,  
261  $\mathcal{G}_{\text{template}}$ , and a to-be-decoded group,  $\mathcal{G}_{\text{decode}}$ . We used Equation 7 to compute a DISFC matrix for each  
262 group ( $\bar{\mathbf{C}}_{\text{template}}$  and  $\bar{\mathbf{C}}_{\text{decode}}$ , respectively). We then correlated the rows of  $\bar{\mathbf{C}}_{\text{template}}$  and  $\bar{\mathbf{C}}_{\text{decode}}$  to form a  
263 number-of-timepoints by number-of-timepoints decoding matrix,  $\Lambda$ . In this way, the rows of  $\Lambda$  reflected  
264 timepoints from the template group, while the columns reflected timepoints from the to-be-decoded group.

265 We used  $\Lambda$  to assign temporal labels to each row  $\bar{\mathbf{C}}_{\text{decode}}$  using the row of  $\bar{\mathbf{C}}_{\text{template}}$  with which it was most  
266 highly correlated. We then repeated this decoding procedure, but using  $\mathcal{G}_{\text{decode}}$  as the template group  
267 and  $\mathcal{G}_{\text{template}}$  as the to-be-decoded group. Given the true timepoint labels (for each group), we defined the  
268 *decoding accuracy* as the average proportion of correctly decoded timepoints, across both groups. We defined  
269 the *relative decoding accuracy* as the difference between the decoding accuracy and chance accuracy (i.e.,  $\frac{1}{T}$ ).

270 **Feature weighting and testing**

271 We sought to examine which types of neural features (i.e., activations, first-order dynamic correlations, and  
272 higher-order dynamic correlations) were informative to the temporal decoders. Using the notation above,  
273 these features correspond to  $\mathbf{X}_0, \mathbf{X}_1, \mathbf{X}_2, \mathbf{X}_3$ , and so on.

274 One challenge to fairly evaluating high-order correlations is that if the kernel used in Equation 4 is  
275 wider than a single timepoint, each repeated application of the equation will result in further temporal  
276 blur. Because our primary assessment metric is temporal decoding accuracy, this unfairly biases against  
277 detecting meaningful signal in higher-order correlations (relative to lower-order correlations). We attempted  
278 to mitigate temporal blur in estimating each  $\mathbf{X}_n$  by using a Dirac  $\delta$  function kernel (which places all of its  
279 mass over a single timepoint; Fig. 3b) to compute each lower-order correlation  $(\mathbf{X}_1, \mathbf{X}_2, \dots, \mathbf{X}_{n-1})$ . We then  
280 used a new (potentially wider, as described below) kernel to compute  $\mathbf{X}_n$  from  $\mathbf{X}_{n-1}$ . In this way, temporal  
281 blurring was applied only in the last step of computing  $\mathbf{X}_n$ . We note that, because each  $\mathbf{X}_n$  is a low-  
282 dimensional representation of the corresponding  $\mathbf{Y}_n$ , the higher-order correlations we estimated reflect true  
283 correlations in the data with lower-fidelity than estimates of lower-order correlations. Therefore, even  
284 after correcting for temporal blurring, our approach is still biased against finding meaningful signal in  
285 higher-order correlations.

286 After computing each  $\mathbf{X}_1, \mathbf{X}_2, \dots, \mathbf{X}_{n-1}$  for each participant, we divided participants into two equally sized  
287 groups ( $\pm 1$  for odd numbers of participants):  $\mathcal{G}_{\text{train}}$  and  $\mathcal{G}_{\text{test}}$ . We then further subdivided  $\mathcal{G}_{\text{train}}$  into  $\mathcal{G}_{\text{train}_1}$   
288 and  $\mathcal{G}_{\text{train}_2}$ . We then computed  $\Lambda$  (temporal correlation) matrices for each type of neural feature, using  $\mathcal{G}_{\text{train}_1}$   
289 and  $\mathcal{G}_{\text{train}_2}$ . This resulted in  $n + 1$   $\Lambda$  matrices (one for the original timeseries of neural activations, and one  
290 for each of  $n$  orders of dynamic correlations). Our objective was to find a set of weights of each of these  
291  $\Lambda$  matrices such that the weighted average of the  $n + 1$  matrices yielded the highest decoding accuracy.  
292 We used quasi-Newton gradient ascent (Nocedal & Wright, 2006), using decoding accuracy (for  $\mathcal{G}_{\text{train}_1}$  and  
293  $\mathcal{G}_{\text{train}_2}$ ) as the objective function to be maximized, to find an optimal set of training data-derived weights,  
294  $\phi_{0,1,\dots,n}$ , where  $\sum_{i=0}^n \phi_i = 1$  and where  $\phi_i \geq 0 \forall i \in [0, 1, \dots, n]$ .

295 After estimating an optimal set of weights, we computed a new set of  $n + 1$   $\Lambda$  matrices correlating the

296 DISFC patterns from  $\mathcal{G}_{\text{train}}$  and  $\mathcal{G}_{\text{test}}$  at each timepoint. We use the resulting decoding accuracy of  $\mathcal{G}_{\text{test}}$   
297 timepoints to estimate how informative the set of neural features containing up to  $n^{\text{th}}$  order correlations  
298 were.

299 We used a permutation-based procedure to form stable estimates of decoding accuracy for each set of  
300 neural features. In particular, we computed the decoding accuracy for each of 10 random group assignments  
301 of  $\mathcal{G}_{\text{train}}$  and  $\mathcal{G}_{\text{test}}$ . We report the mean accuracy (along with 95% confidence intervals) for each set of neural  
302 features.

303 **Identifying robust decoding results**

304 The temporal decoding procedure we use to estimate which neural features support ongoing cognitive  
305 processing is governed by several parameters. In particular, Equation 4 requires defining a kernel function,  
306 which can take on different shapes and widths. For a fixed set of neural features, each of these parameters  
307 can yield different decoding accuracies. Further, the best decoding accuracy for a given timepoint may be  
308 reliably achieved by one set of parameters, whereas the best decoding accuracy for another timepoint might  
309 be reliably achieved by a different set of parameters, and the best decoding accuracy across *all* timepoints  
310 might be reliably achieved by still another different set of parameters. Rather than attempting to maximize  
311 decoding accuracy, we sought to discover the trends in the data that were robust to classifier parameters  
312 choices. Specifically, we sought to characterize how decoding accuracy varied (under different experimental  
313 conditions) as a function of which neural features were considered.

314 To identify decoding results that were robust to specific classifier parameter choices, we repeated our  
315 decoding analyses after substituting in each of a variety of kernel shapes and widths for Equation 4. We  
316 examined Gaussian (Fig. 3c), Laplace (Fig. 3d), and Mexican Hat (Fig. 3e) kernels, each with widths of 5, 10,  
317 20, and 50 samples. We then report the average decoding accuracies across all of these parameter choices.  
318 This enabled us to (partially) factor out performance characteristics that were parameter-dependent, within  
319 the set of parameters we examined.

320 **Reverse inference**

321 The dynamic patterns we examined comprise high-dimensional correlation patterns at each timepoint. To  
322 help interpret the resulting patterns in the context of other studies, we created summary maps by computing  
323 the across-timepoint average pairwise correlations at each order of analysis (first order, second order, etc.).  
324 We selected the 10 strongest (absolute value) correlations at each order. Each correlation is between the  
325 dynamic activity patterns (or patterns of dynamic high-order correlations) measured at two RBF nodes

326 (see *Hierarchical Topographic Factor Analysis*). Therefore, the 10 strongest correlations involved up to 20 RBF  
327 nodes. Each RBF defines a spatial function whose activations range from 0 to 1. We thresholded each  
328 RBF at 0.999 to construct a map of spherical components that denoted the endpoints of the 10 strongest  
329 correlations. We then carried out a meta analysis using Neurosynth (Rubin et al., 2017) to identify the 10  
330 terms most commonly associated with the given map. This resulted in a set of 10 terms associated with the  
331 average dynamic correlation patterns at each order.

## 332 Results

333 We sought to understand whether high-level cognition is supported by dynamic patterns of high-order  
334 correlations. To that end, we developed a computational framework for estimating the dynamics of high-  
335 order correlations in multivariate timeseries data (see *Dynamic inter-subject functional connectivity (DISFC)*  
336 and *Dynamic higher-order correlations*). We evaluated the efficacy of this framework at recovering known  
337 patterns in several synthetic datasets (see *Synthetic data*). We then applied the framework to a public  
338 fMRI dataset collected as participants listened to an auditorily presented story, listened to a temporally  
339 scrambled version of the story, or underwent a resting state scan (see *Functional neuroimaging data collected*  
340 *during story listening*). We used the relative decoding accuracies of classifiers trained on different sets of  
341 neural features to estimate which types of features reflected ongoing cognitive processing.

### 342 Recovering known dynamic correlations from synthetic data

343 We generated synthetic datasets that differed in how the underlying correlations changed over time. For  
344 each dataset, we applied Equation 4 with a variety of kernel shapes and widths. We assessed how well  
345 the true underlying correlations at each timepoint matched the recovered correlations (Fig. 4). For every  
346 kernel and dataset we tested, our approach recovered the correlation dynamics we embedded into the data.  
347 However, the quality of these recoveries varied across different synthetic datasets in a kernel-dependent  
348 way.

349 In general, wide monotonic kernel shapes (Laplace, Gaussian), and wider kernels (within a shape),  
350 performed best when the correlations varied gradually from moment-to-moment (Figs. 4a, c, and d). In the  
351 extreme, as the rate of change in correlations approaches 0 (Fig. 4a), an infinitely wide kernel would exactly  
352 recover the Pearson's correlation (e.g., compare Eqns. 2 and 4).

353 When the correlation dynamics were unstructured in time (Fig. 4b), a Dirac  $\delta$  kernel (infinitely narrow)  
354 performed best. This is because, when every timepoint's correlations are independent of the correlations at

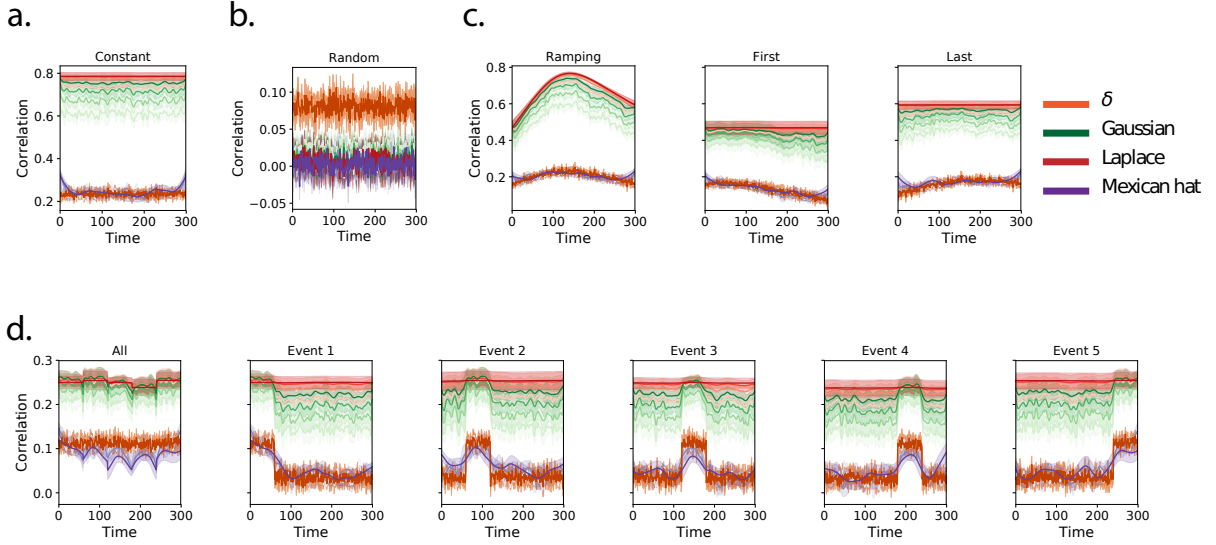


**Figure 4: Recovering known dynamic correlations from synthetic data.** Each panel displays the average correlations between the vectorized upper triangles of the recovered correlation matrix at each timepoint and either the true underlying correlation at each timepoint or a reference correlation matrix. (The averages are taken across 10 different randomly generated synthetic datasets of the given category.) Error ribbons denote 95% confidence intervals (taken across datasets). Different colors denote different kernel shapes, and the shading within each color family denotes the kernel width parameter. For a complete description of each synthetic dataset, see *Synthetic data*. **a. Constant correlations.** These datasets have a stable (unchanging) underlying correlation matrix. **b. Random correlations.** These datasets are generated using a new independently drawn correlation matrix at each new timepoint. **c. Ramping correlations.** These datasets are generated by smoothly varying the underlying correlations between the randomly drawn correlation matrices at first and last timepoints. The left panel displays the correlations between the recovered dynamic correlations and the underlying ground truth correlations. The middle panel compares the recovered correlations with the *first* timepoint’s correlation matrix. The right panel compares the recovered correlations with the *last* timepoint’s correlation matrix. **d. Event-based correlations.** These datasets are each generated using five randomly drawn correlation matrices that each remain stable for a fifth of the total timecourse. The left panel displays the correlations between the recovered dynamic correlations and the underlying ground truth correlations. The right panels compare the recovered correlations with the correlation matrices unique to each event.

355 every other timepoint, averaging data over time dilutes the available signal. Following a similar pattern,  
356 holding kernel shape fixed, narrower kernel parameters better recovered randomly varying correlations.

### 357 Cognitively relevant dynamic high-order correlations in fMRI data

358 We used across-participant temporal decoders to identify cognitively relevant neural patterns in fMRI data  
359 (see *Forward inference and decoding accuracy*). The dataset we examined (collected by Simony et al., 2016)  
360 comprised four experimental conditions that exposed participants to stimuli that varied systematically in  
361 how cognitively engaging they were. The *intact* experimental condition had participants listen to an audio  
362 recording of a 10-minute story. The *paragraph*-scrambled experimental condition had participants listen to a  
363 temporally scrambled version of the story, where the paragraphs occurred out of order (but where the same  
364 total set of paragraphs were presented over the full listening interval). All participants in this condition  
365 experienced the scrambled paragraphs in the same order. The *word*-scrambled experimental condition had  
366 participants listen to a temporally scrambled version of the story where the words in the story occurred in a  
367 random order. All participants in the word conditions experienced the scrambled words in the same order.  
368 Finally, in a *rest* experimental condition, participants lay in the scanner with no overt stimulus, with their  
369 eyes open (blinking as needed). This dataset provided a convenient means of testing our hypothesis that  
370 different levels of cognitive processing and engagement are supported by different orders of brain activity  
371 dynamics.

372 In brief, we computed timeseries of dynamic high-order correlations that were similar across participants  
373 in each of two randomly assigned groups: a training group and a test group. We then trained classifiers  
374 on the training group's data to match each sample from the test group with a stimulus timepoint. Each  
375 classifier comprised a weighted blend of neural patterns that reflected up to  $n^{\text{th}}$ -order dynamic correlations  
376 (see *Feature weighting and testing*). We repeated this process for  $n \in \{0, 1, 2, \dots, 10\}$ . Our examinations of  
377 synthetic data suggested that none of the kernels we examined were "universal" in the sense of optimally  
378 recovering underlying correlations regardless of the structure of those correlations. We found a similar  
379 pattern in the (real) fMRI data, whereby different kernels yielded different decoding accuracies, but no  
380 single kernel emerged as the clear "best." In our analyses of neural data, we therefore averaged our  
381 decoding results over a variety of kernel shapes and widths in order to identify results that were robust to  
382 specific kernel parameters (see *Identifying robust decoding results*).

383 Our approach to estimating dynamic high-order correlations entails mapping the high-dimensional  
384 feature space of correlations (a  $T$  by  $O(K^2)$  matrix) onto a lower-dimensional  $T$  by  $K$  matrix. We carried out  
385 two sets of analyses that differed in how this mapping was computed. The first set of analyses used PCA

386 to find a low-dimensional embedding of the original dynamic correlation matrices (Fig. 5a,b). The second  
387 set of analyses characterized correlations in dynamics of each feature's eigenvector centrality, but did not  
388 preserve the underlying activity dynamics (Fig. 5c,d).

389 Both sets of temporal decoding analyses yielded qualitatively similar results for the auditory (non-  
390 rest) conditions of the experiment (Fig. 5: pink, yellow, and teal lines). The highest decoding accuracy  
391 for participants who listened to the intact (unscrambled) story was achieved using high-order dynamic  
392 correlations (PCA: second-order; eigenvector-centrality: fourth-order). Scrambled versions of the story were  
393 best decoded by lower-order correlations (PCA/paragraph: first-order; PCA/word: order zero; eigenvector  
394 centrality/paragraph: order zero; eigenvector centrality/word: order zero). The two sets of analyses yielded  
395 different decoding results on resting state data (Fig. 5: purple lines). We note that while the resting state  
396 times could be decoded reliably, the accuracies were only very slightly above chance. We speculate that the  
397 decoders might have picked up on attentional drift, boredom, or tiredness; we hypothesize that these all  
398 increased throughout the resting state scan. The decoders might be picking up on aspects of these loosely  
399 defined cognitive states that are common across individuals. The PCA-based approach achieved the highest  
400 resting state decoding accuracy using order zero features (non-correlational, activation-based), whereas the  
401 eigenvector centrality-based approach achieved the highest resting state decoding accuracy using second-  
402 order correlations. Taken together, these analyses indicate that high-level cognitive processing (while  
403 listening to the intact story) is reflected in the dynamics of high-order correlations in brain activity, whereas  
404 lower-level cognitive processing (while listening to scrambled versions of the story that lack rich meaning) is  
405 reflected in the dynamics of lower-order correlations and non-correlational activity dynamics. Further, these  
406 patterns are associated both with the underlying activity patterns (characterized using PCA) and also with  
407 the changing relative positions that different brain areas occupy in their associated networks (characterized  
408 using eigenvector centrality).

409 Having established that patterns of high-order correlations are informative to decoders, we next won-  
410 dered which specific networks of brain regions contributed most to these patterns. As a representative  
411 example, we selected the kernel parameters that yielded decoding accuracies that best matched the average  
412 accuracies across all of the kernel parameters we examined. Using Figure 5c as a template, the best-matching  
413 kernel was a Laplace kernel with a width of 50 (Fig. 3d). We used this kernel to compute a single  $K$  by  $K$   
414  $n^{\text{th}}$ -order DISFC matrix for each experimental condition. We then used Neurosynth (Rubin et al., 2017) to  
415 compute the terms most highly associated with the most strongly correlated pairs of regions in each of these  
416 matrices (Fig. 6; see *Reverse inference*).

417 For all of the story listening conditions (intact, paragraph, and word), we found that first- and second-  
418 order correlations were most strongly associated with auditory and speech processing areas. During

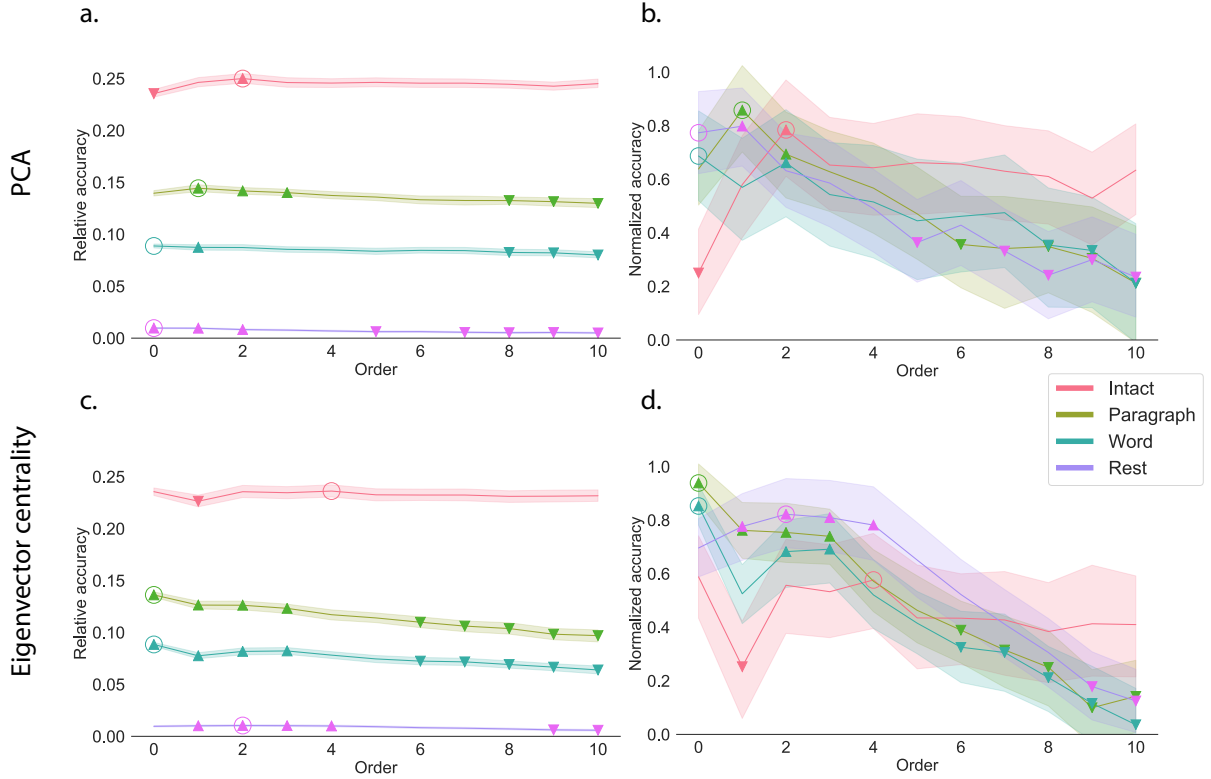


**Figure 5: Across-participant decoding accuracy varies with correlation order and cognitive engagement.**

**a. Decoding accuracy as a function of order: PCA.** Order (x-axis) refers to the maximum order of dynamic correlations that were available to the classifiers (see *Feature weighting and testing*). The reported across-participant decoding accuracies are averaged over all kernel shapes and widths (see *Identifying robust decoding results*). The y-values are displayed relative to chance accuracy (intact:  $\frac{1}{300}$ ; paragraph:  $\frac{1}{272}$ ; word:  $\frac{1}{300}$ ; rest:  $\frac{1}{400}$ ). The error bars denote 95% confidence intervals across cross-validation folds (i.e., random assignments of participants to the training and test sets). The colors denote the experimental condition. Arrows denote sets of features that yielded reliably higher (upwards facing) or lower (downward facing) decoding accuracy than the mean of all other features (via a two-tailed test, thresholded at  $p < 0.05$ ). Figure S1 displays additional comparisons between the decoding accuracies achieved using different sets of neural features. The circled values represent the maximum decoding accuracy within each experimental condition.

**b. Normalized decoding accuracy as a function of order: PCA.** This panel displays the same results as Panel a, but here each curve has been normalized to have a maximum value of 1 and a minimum value of 0 (including the upper and lower bounds of the respective 95% confidence intervals). Panels a and b used PCA to project each high-dimensional pattern of dynamic correlations onto a lower-dimensional space.

**c. Decoding accuracy as a function of order: eigenvector centrality.** This panel is in the same format as Panel a, but here eigenvector centrality has been used to project the high-dimensional patterns of dynamic correlations onto a lower-dimensional space.

**d. Normalized decoding accuracy as a function of order: eigenvector centrality.** This panel is in the same format as Panel b, but here eigenvector centrality has been used to project the high-dimensional patterns of dynamic correlations onto a lower-dimensional space.

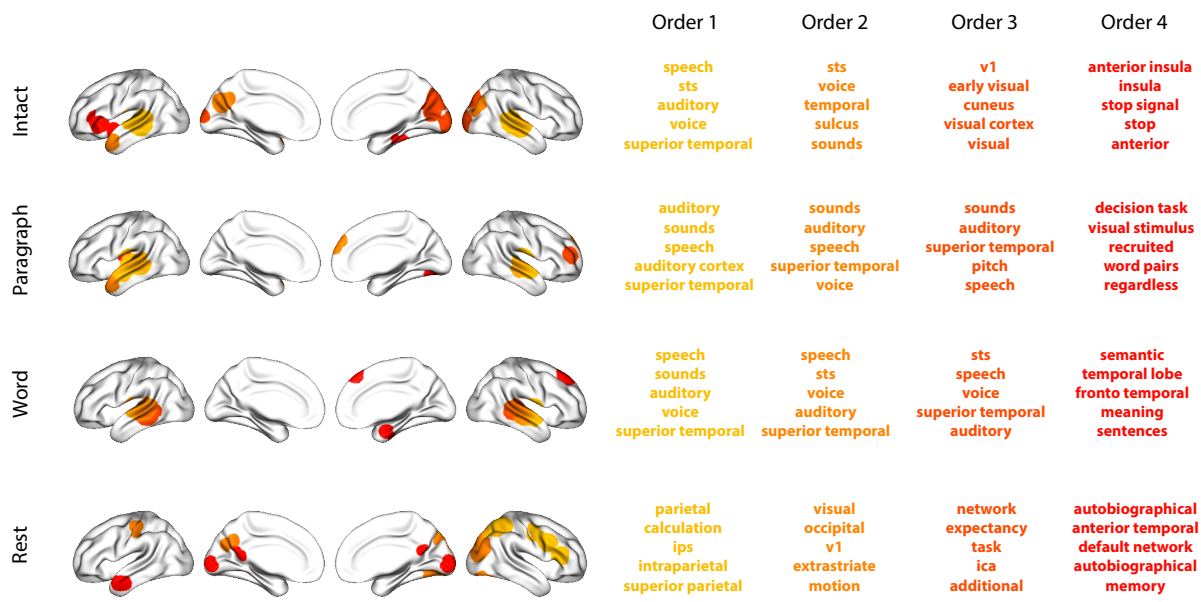


**Figure 6: Top terms associated with the endpoints of the strongest correlations.** Each color corresponds to one order of inter-subject functional correlations. The inflated brain plots display the locations of the endpoints of the 10 strongest (absolute value) correlations at each order, projected onto the cortical surface (Combrisson et al., 2019). The lists of terms on the right display the top five Neurosynth terms (Rubin et al., 2017) decoded from the corresponding brain maps for each order. Each row displays data from a different experimental condition. Additional maps and their corresponding Neurosynth terms may be found in the *Supplementary materials* (intact: Figure S2; paragraph: Figure S3; word: Figure S4; rest: Figure S5).

419 intact story listening, third-order correlations reflected integration with visual areas, and fourth-order  
420 correlations reflected integration with areas associated with high-level cognition and cognitive control,  
421 such as the ventrolateral prefrontal cortex. However, during listening to temporally scrambled stories,  
422 these higher-order correlations instead involved interactions with additional regions associated with speech  
423 and semantic processing. By contrast, we found a much different set of patterns in the resting state data.  
424 First-order resting state correlations were most strongly associated with regions involved in counting and  
425 numerical understanding. Second-order resting state correlations were strongest in visual areas; third-order  
426 correlations were strongest in task-positive areas; and fourth-order correlations were strongest in regions  
427 associated with autobiographical and episodic memory. We carried out analogous analyses to create maps  
428 (and decode the top associated Neurosynth terms) for up to fifteenth-order correlations (Figs. S2, S3, S4, and  
429 S5). Of note, examining fifteenth-order correlations between 700 nodes using conventional methods would  
430 have required storing roughly  $\frac{700^{2 \times 15}}{2} \approx 1.13 \times 10^{85}$  floating point numbers—assuming single-precision (32  
431 bits each), this would require roughly 32 times as many bits as there are molecules in the known universe!  
432 Although these fifteenth-order correlations do appear (visually) to have some well-formed structure, we  
433 provide this latter example primarily as a demonstration of the efficiency and scalability of our approach.

## 434 Discussion

435 We tested the hypothesis that high-level cognition is supported by high-order brain network dynamics (e.g.,  
436 see Reimann et al., 2017; Solomon et al., 2019). We examined high-order network dynamics in functional  
437 neuroimaging data collected during a story listening experiment. When participants listened to an auditory  
438 recording of the story, participants exhibited similar high-order brain network dynamics. By contrast,  
439 when participants instead listened to temporally scrambled recordings of the story, only lower-order brain  
440 network dynamics were similar across participants. Our results indicate that higher orders of network  
441 interactions support higher-level aspects of cognitive processing (Fig. 7).

442 The notion that cognition is reflected in (and possibly mediated by) patterns of first-order network  
443 dynamics has been suggested by or proposed in myriad empirical studies and reviews (e.g., Chang &  
444 Glover, 2010; Demertzi et al., 2019; Fong et al., 2019; Gonzalez-Castillo et al., 2019; Liégeois et al., 2019; Lurie  
445 et al., 2018; Park et al., 2018; Preti et al., 2017; Roy et al., 2019; Turk-Browne, 2013; Zou et al., 2019). Our study  
446 extends this line of work by finding cognitively relevant *higher-order* network dynamics that reflect ongoing  
447 cognition. Our findings complement other work that uses graph theory and topology to characterize how  
448 brain networks reconfigure during cognition (e.g., Bassett et al., 2006; Betzel et al., 2019; McIntosh & Jirsa,  
449 2019; Reimann et al., 2017; Sizemore et al., 2018; Toker & Sommer, 2019; Zheng et al., 2019).

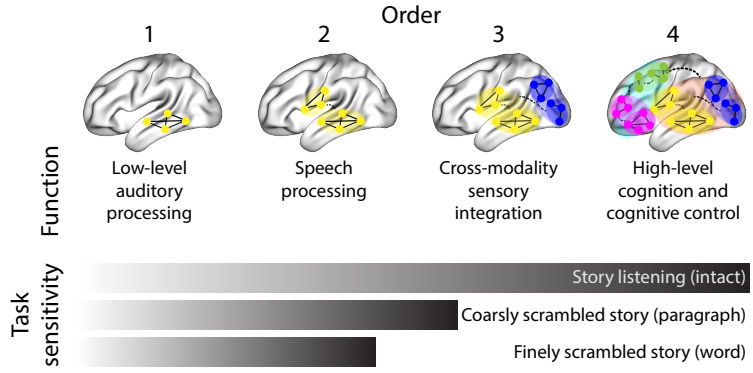


**Figure 7: Proposed high-order network dynamics underlying high-level cognition during story listening.** Higher orders of network interactions support higher-level aspects of cognitive processing. When tasks evoke richer, deeper, and/or higher-level processing, this is reflected in higher-order network interactions.

450 An open question not addressed by our study pertains to how different structures integrate incoming  
 451 information with different time constants. For example, one line of work suggests that the cortical surface  
 452 comprises a structured map such that nearby brain structures process incoming information at similar  
 453 timescales. Low-level sensory areas integrate information relatively quickly, whereas higher-level regions  
 454 integrate information relatively slowly (Baldassano et al., 2017; Hasson et al., 2015, 2008; Honey et al., 2012;  
 455 Lerner et al., 2014, 2011). Other related work in human and mouse brains indicates that the temporal  
 456 response profile of a given brain structure may relate to how strongly connected that structure is with other  
 457 brain areas (Fallon et al., 2019). Further study is needed to understand the role of temporal integration at  
 458 different scales of network interaction, and across different anatomical structures.

459 Another potential limitation of our approach relates to recent work suggesting that the brain undergoes  
 460 rapid state changes, for example across event boundaries (e.g., Baldassano et al., 2017). Shappell et al.  
 461 (2019) used hidden semi-Markov models to estimate state-specific network dynamics (also see Vidaurre et  
 462 al., 2018). Our general approach might be extended by considering putative state transitions. For example,  
 463 rather than weighting all timepoints using a similar kernel (Eqn. 4), the kernel function could adapt on a  
 464 timepoint-by-timepoint basis such that only timepoints determined to be in the same “state” were given  
 465 non-zero weight.

466 Identifying higher-order network dynamics associated with high-level cognition required several im-  
 467 portant methods advances. First, we used kernel-based dynamic correlations to extended the notion of  
 468 (static) inter-subject functional connectivity (Simony et al., 2016) to a dynamic measure of inter-subject func-  
 469 tional connectivity (DISFC) that does not rely on sliding windows, and that may be computed at individual  
 470 timepoints. This allowed us to precisely characterize stimulus-evoked network dynamics that were similar  
 471 across individuals. Second, we developed a computational framework for efficiently and scalably estimat-

472 ing high-order dynamic correlations. Our approach uses dimensionality reduction algorithms and graph  
473 measures to obtain low-dimensional embeddings of patterns of network dynamics. Third, we developed  
474 an analysis framework for identifying robust decoding results by carrying out our analyses using a range  
475 of parameter values and then identifying which results were robust to specific parameter choices.

476 **Concluding remarks**

477 The complex hierarchy of dynamic interactions that underlie our thoughts is perhaps the greatest mystery in  
478 modern science. Methods for characterizing the dynamics of high-order correlations in neural data provide  
479 a window into the neural basis of cognition. By showing that high-level cognition is reflected in high-order  
480 network dynamics, we have elucidated the next step on the path towards understanding the neural basis  
481 of cognition.

482 **Acknowledgements**

483 We acknowledge discussions with Luke Chang, Vassiki Chauhan, Hany Farid, Paxton Fitzpatrick, Andrew  
484 Heusser, Eshin Jolly, Aaron Lee, Qiang Liu, Matthijs van der Meer, Judith Mildner, Gina Notaro, Stephen  
485 Satterthwaite, Emily Whitaker, Weizhen Xie, and Kirsten Ziman. Our work was supported in part by NSF  
486 EPSCoR Award Number 1632738 to J.R.M. and by a sub-award of DARPA RAM Cooperative Agreement  
487 N66001-14-2-4-032 to J.R.M. The content is solely the responsibility of the authors and does not necessarily  
488 represent the official views of our supporting organizations.

489 **Author contributions**

490 Concept: J.R.M. Implementation: T.H.C., L.L.W.O., and J.R.M. Analyses: L.L.W.O. and J.R.M. Writing:  
491 L.L.W.O. and J.R.M.

492 **References**

- 493 Allen, E. A., Damaraju, E., Plis, S. M., Erhardt, E. B., Eichele, T., & Calhoun, V. D. (2012). Tracking  
494 whole-brain connectivity dynamics in the resting state. *Cerebral Cortex*, 24(3), 663–676.
- 495 Alvarez-Hamelin, I., Dall'Asta, L., Barrat, A., & Vespignani, A. (2005). *k*-corr decomposition: a tool for the  
496 visualization of large scale networks. *arXiv*, cs/0504107v2.

- 497 Baldassano, C., Chen, J., Zadbood, A., Pillow, J. W., Hasson, U., & Norman, K. A. (2017). Discovering event  
498 structure in continuous narrative perception and memory. *Neuron*, 95(3), 709–721.
- 499 Barthélémy, M. (2004). Betweenness centrality in large complex networks. *European Physical Journal B*, 38,  
500 163–168.
- 501 Bassett, D., Meyer-Lindenberg, A., Achard, S., Duke, T., & Bullmore, E. (2006, December). Adaptive  
502 reconfiguration of fractal small-world human brain functional networks. *Proceedings of the National  
503 Academy of Sciences, USA*, 103(51), 19518–23.
- 504 Betzel, R. F., Byrge, L., Esfahlani, F. Z., & Kennedy, D. P. (2019). Temporal fluctuations in the brain's modular  
505 architecture during movie-watching. *bioRxiv*, doi.org/10.1101/750919.
- 506 Bonacich, P. (2007). Some unique properties of eigenvector centrality. *Social Networks*, 29(4), 555–564.
- 507 Bullmore, E., & Sporns, O. (2009). Complex brain networks: graph theoretical analysis of structural and  
508 functional systems. *Nature Reviews Neuroscience*, 10(3), 186–198.
- 509 Capota, M., Turek, J., Chen, P.-H., Zhu, X., Manning, J. R., Sundaram, N., ... Shin, Y. S. (2017). *Brain imaging  
510 analysis kit*. Retrieved from <https://doi.org/10.5281/zenodo.59780>
- 511 Chang, C., & Glover, G. H. (2010). Time-frequency dynamics of resting-state brain connectivity measured  
512 with fMRI. *NeuroImage*, 50, 81–98.
- 513 Christakis, N. A., & Fowler, J. H. (2010). Social network sensors for early detection of contagious outbreaks.  
514 *PLoS One*, 5(9), e12948.
- 515 Combrisson, E., Vallat, R., O'Reilly, C., Jas, M., Pasarella, A., l Saive, A., ... Jerbi, K. (2019). Visbrain: a  
516 multi-purpose GPU-accelerated open-source suite for multimodal brain data visualization. *Frontiers in  
517 Neuroinformatics*, 13(14), 1–14.
- 518 Comon, P., Jutten, C., & Herault, J. (1991). Blind separation of sources, part II: Problems statement. *Signal  
519 Processing*, 24(1), 11 - 20.
- 520 Demertzi, A., Tagliazucchi, E., Dehaene, S., Deco, G., Barttfeld, P., Raimondo, F., ... Sitt, J. D. (2019). Human  
521 consciousness is supported by dynamic complex patterns of brain signal coordination. *Science Advances*,  
522 5(2), eaat7603.
- 523 Estrada, E., & Rodríguez-Velázquez, J. A. (2005). Subgraph centrality in complex networks. *Physical Review  
524 E*, 71(5), 056103.

- 525 Etzel, J. A., Gazzola, V., & Keysers, C. (2009). An introduction to anatomical ROI-based fMRI classification.  
526 *Brain Research*, 1282, 114–125.
- 527 Fallon, J., Ward, P., Parkes, L., Oldham, S., Arnatkevičiūtė, A., Fornito, A., & Fulcher, B. D. (2019).  
528 Timescales of spontaneous activity fluctuations relate to structural connectivity in the brain. *bioRxiv*,  
529 [doi.org/10.1101/655050](https://doi.org/10.1101/655050).
- 530 Fong, A. H. C., Yoo, K., Rosenberg, M. D., Zhang, S., Li, C.-S. R., Scheinost, D., ... Chun, M. M. (2019).  
531 Dynamic functional connectivity during task performance and rest predicts individual differences in  
532 attention across studies. *NeuroImage*, 188, 14–25.
- 533 Freeman, L. C. (1977). A set of measures of centrality based on betweenness. *Sociometry*, 40(1), 35–41.
- 534 Geisberger, R., Sanders, P., & Schultes, D. (2008). Better approximation of betweenness centrality. *Proceedings*  
535 *of the meeting on Algorithm Engineering and Experiments*, 90–100.
- 536 Gershman, S., Blei, D., Pereira, F., & Norman, K. (2011). A topographic latent source model for fMRI data.  
537 *NeuroImage*, 57, 89–100.
- 538 Gonzalez-Castillo, J., Caballero-Gaudes, C., Topolski, N., Handwerker, D. A., Pereira, F., & Bandettini, P. A.  
539 (2019). Imaging the spontaneous flow of thought: distinct periods of cognition contribute to dynamic  
540 functional connectivity during rest. *NeuroImage*, 202(116129).
- 541 Halu, A., Mondragón, R. J., Panzarasa, P., & Bianconi, G. (2013). Multiplex PageRank. *PLoS One*, 8(10),  
542 e78293.
- 543 Hasson, U., Chen, J., & Honey, C. J. (2015). Hierarchical process memory: memory as an integral component  
544 of information processing. *Trends in Cognitive Science*, 19(6), 304–315.
- 545 Hasson, U., Yang, E., Vallines, I., Heeger, D. J., & Rubin, N. (2008). A hierarchy of temporal receptive windows  
546 in human cortex. *Journal of Neuroscience*, 28(10), 2539–2550. doi: 10.1523/JNEUROSCI.5487-07.2008
- 547 Haxby, J. V., Gobbini, M. I., Furey, M. L., Ishai, A., Schouten, J. L., & Pietrini, P. (2001). Distributed and  
548 overlapping representations of faces and objects in ventral temporal cortex. *Science*, 293, 2425–2430.
- 549 Hinton, G. E., & Salakhutdinov, R. R. (2006). Reducing the dimensionality of data with neural networks.  
550 *Science*, 313(5786), 504–507.
- 551 Honey, C. J., Kotter, R., Breakspear, M., & Sporns, O. (2007). Network structure of cerebral cortex shapes  
552 functional connectivity on multiple time scales. *Proceedings of the National Academy of Science USA*, 104(24),  
553 10240–10245.

- 554 Honey, C. J., Thesen, T., Donner, T. H., Silbert, L. J., Carlson, C. E., Devinsky, O., ... Hasson, U. (2012). Slow  
555 cortical dynamics and the accumulation of information over long timescales. *Neuron*, 76, 423-434. doi:  
556 10.1016/j.neuron.2012.08.011
- 557 Huth, A. G., de Heer, W. A., Griffiths, T. L., Theunissen, F. E., & Gallant, J. L. (2016). Natural speech reveals  
558 the semantic maps that tile human cerebral cortex. *Nature*, 532, 453–458.
- 559 Huth, A. G., Nisimoto, S., Vu, A. T., & Gallant, J. L. (2012). A continuous semantic space describes  
560 the representation of thousands of object and action categories across the human brain. *Neuron*, 76(6),  
561 1210-1224.
- 562 Jutten, C., & Herault, J. (1991). Blind separation of sources, part I: An adaptive algorithm based on  
563 neuromimetic architecture. *Signal Processing*, 24(1), 1–10.
- 564 Kamitani, Y., & Tong, F. (2005). Decoding the visual and subjective contents of the human brain. *Nature*  
565 *Neuroscience*, 8, 679–685.
- 566 Landau, E. (1895). Zur relativen Wertbemessung der Turnierresultate. *Deutsches Wochenschach*, 11, 366–369.
- 567 Lee, D. D., & Seung, H. S. (1999). Learning the parts of objects by non-negative matrix factorization. *Nature*,  
568 401, 788–791.
- 569 Lerner, Y., Honey, C. J., Katkov, M., & Hasson, U. (2014). Temporal scaling of neural responses to compressed  
570 and dilated natural speech. *Journal of Neurophysiology*, 111, 2433–2444.
- 571 Lerner, Y., Honey, C. J., Silbert, L. J., & Hasson, U. (2011). Topographic mapping of a hierarchy of  
572 temporal receptive windows using a narrated story. *Journal of Neuroscience*, 31(8), 2906-2915. doi: 10.1523/  
573 JNEUROSCI.3684-10.2011
- 574 Liégeois, R., Li, J., Kong, R., Orban, C., De Ville, D. V., Ge, T., ... Yeo, B. T. T. (2019). Resting brain  
575 dynamics at different timescales capture distinct aspects of human behavior. *Nature Communications*,  
576 10(2317), doi.org/10.1038/s41467-019-10317-7.
- 577 Lin, J. (2009). Divergence measures based on the Shannon entropy. *IEEE Transactions on Information Theory*,  
578 37(1), 145–151.
- 579 Lohmann, G., Margulies, D. S., Horstmann, A., Pleger, B., Lepsien, J., Goldhahn, D., ... Turner, R. (2010).  
580 Eigenvector centrality mapping for analyzing connectivity patterns in fMRI data of the human brain.  
581 *PLoS One*, 5(4), e10232.

- 582 Lurie, D., Kessler, D., Bassett, D., Betzel, R., Breakspear, M., Keilholz, S., ... Calhoun, V. (2018). On the  
583 nature of time-varying functional connectivity in resting fMRI. *PsyArXiv*, doi.org/10.31234/osf.io/xtzre.
- 584 Mack, M. L., Preston, A. R., & Love, B. C. (2017). Medial prefrontal cortex compresses concept representations  
585 through learning. *bioRxiv*, doi.org/10.1101/178145.
- 586 Mairal, J., Ponce, J., Sapiro, G., Zisserman, A., & Bach, F. R. (2009). Supervised dictionary learning. *Advances*  
587 in *Neural Information Processing Systems*, 1033–1040.
- 588 Mairal, J. B., Bach, F., Ponce, J., & Sapiro, G. (2009). Online dictionary learning for sparse coding. *Proceedings*  
589 of the 26th annual international conference on machine learning, 689–696.
- 590 Manning, J. R., Ranganath, R., Norman, K. A., & Blei, D. M. (2014). Topographic factor analysis: a Bayesian  
591 model for inferring brain networks from neural data. *PLoS One*, 9(5), e94914.
- 592 Manning, J. R., Zhu, X., Willke, T. L., Ranganath, R., Stachenfeld, K., Hasson, U., ... Norman, K. A. (2018).  
593 A probabilistic approach to discovering dynamic full-brain functional connectivity patterns. *NeuroImage*,  
594 180, 243–252.
- 595 McInnes, L., & Healy, J. (2018). UMAP: Uniform manifold approximation and projection for dimension  
596 reduction. *arXiv*, 1802(03426).
- 597 McIntosh, A. R., & Jirsa, V. K. (2019). The hidden repertoire of brain dynamics and dysfunction. *Network*  
598 *Neuroscience*, doi.org/10.1162/netn\_a\_00107.
- 599 Mitchell, T., Shinkareva, S., Carlson, A., Chang, K., Malave, V., Mason, R., & Just, M. (2008). Predicting  
600 human brain activity associated with the meanings of nouns. *Science*, 320(5880), 1191.
- 601 Newman, M. E. J. (2005). A measure of betweenness centrality based on random walks. *Social Networks*, 27,  
602 39–54.
- 603 Newman, M. E. J. (2008). The mathematics of networks. *The New Palgrave Encyclopedia of Economics*, 2, 1–12.
- 604 Nishimoto, S., Vu, A., Naselaris, T., Benjamini, Y., Yu, B., & Gallant, J. (2011). Reconstructing visual  
605 experience from brain activity evoked by natural movies. *Current Biology*, 21, 1 - 6.
- 606 Nocedal, J., & Wright, S. J. (2006). *Numerical optimization*. New York: Springer.
- 607 Norman, K. A., Newman, E., Detre, G., & Polyn, S. M. (2006). How inhibitory oscillations can train neural  
608 networks and punish competitors. *Neural Computation*, 18, 1577–1610.

- 609 Opsahl, T., Agneessens, F., & Skvoretz, J. (2010). Node centrality in weighted networks: generalizing degree  
610 and shortest paths. *Social Networks*, 32, 245–251.
- 611 Park, H.-J., Friston, K. J., Pae, C., Park, B., & Razi, A. (2018). Dynamic effective connectivity in resting state  
612 fMRI. *NeuroImage*, 180, 594–608.
- 613 Pearson, K. (1901). On lines and planes of closest fit to systems of points in space. *The London, Edinburgh,  
614 and Dublin Philosophical Magazine and Journal of Science*, 2, 559–572.
- 615 Pereira, F., Lou, B., Pritchett, B., Ritter, S., Gershman, S. J., Kanwisher, N., ... Fedorenko, E. (2018). Toward  
616 a universal decoder of linguistic meaning from brain activation. *Nature Communications*, 9(963), 1–13.
- 617 Preti, M. G., Bolton, T. A. W., & Van De Ville, D. (2017). The dynamic functional connectome: state-of-the-art  
618 and perspectives. *NeuroImage*, 160, 41–54.
- 619 Rao, C. R. (1982). Diversity and dissimilarity coefficients: a unified approach. *Theoretical Population Biology*,  
620 21(1), 24–43.
- 621 Reimann, M. W., Nolte, M., Scolamiero, M., Turner, K., Perin, R., Chindemi, G., ... Markram, H. (2017).  
622 Cliques of neurons bound into cavities provide a missing link between structure and function. *Frontiers  
623 in Computational Neuroscience*, 11(48), 1–16.
- 624 Ricotta, C., & Szeidl, L. (2006). Towards a unifying approach to diversity measures: Bridging the gap  
625 between the Shannon entropy and Rao's quadratic index. *Theoretical Population Biology*, 70(3), 237–243.
- 626 Roy, D. S., Park, Y.-G., Ogawa, S. K., Cho, J. H., Choi, H., Kamensky, L., ... Tonegawa, S. (2019). Brain-  
627 wide mapping of contextual fear memory engram ensembles supports the dispersed engram complex  
628 hypothesis. *bioRxiv*, doi.org/10.1101/668483.
- 629 Rubin, T. N., Kyoejo, O., Gorgolewski, K. J., Jones, M. N., Poldrack, R. A., & Yarkoni, T. (2017). Decoding  
630 brain activity using a large-scale probabilistic functional-anatomical atlas of human cognition. *PLoS  
631 Computational Biology*, 13(10), e1005649.
- 632 Rubinov, M., & Sporns, O. (2010). Complex network measures of brain connectivity: uses and interpreta-  
633 tions. *NeuroImage*, 52, 1059–1069.
- 634 Schreiber, T. (2000). Measuring information transfer. *Physical Review Letters*, 85(2), 461–464.
- 635 Shappell, H., Caffo, B. S., Pekar, J. J., & Lindquist, M. A. (2019). Improved state change estimation in  
636 dynamic functional connectivity using hidden semi-Markov models. *NeuroImage*, 191, 243–257.

- 637 Simony, E., Honey, C. J., Chen, J., & Hasson, U. (2016). Uncovering stimulus-locked network dynamics  
638 during narrative comprehension. *Nature Communications*, 7(12141), 1–13.
- 639 Sizemore, A. E., Giusti, C., Kahn, A., Vettel, J. M., Betzel, R. F., & Bassett, D. S. (2018). Cliques and cavities  
640 in the human connectome. *Journal of Computational Neuroscience*, 44(1), 115–145.
- 641 Solomon, S. H., Medaglia, J. D., & Thompson-Schill, S. L. (2019). Implementing a concept network model.  
642 *Behavior Research Methods*, 51, 1717–1736.
- 643 Spearman, C. (1904). General intelligence, objectively determined and measured. *American Journal of  
644 Psychology*, 15, 201–292.
- 645 Sporns, O., & Honey, C. J. (2006). Small worlds inside big brains. *Proceedings of the National Academy of  
646 Science USA*, 103(51), 19219–19220.
- 647 Thompson, W. H., Richter, C. G., Plavén-Sigray, P., & Fransson, P. (2018). Simulations to benchmark  
648 time-varying connectivity methods for fMRI. *PLoS Computational Biology*, 14(5), e1006196.
- 649 Tipping, M. E., & Bishop, C. M. (1999). Probabilistic principal component analysis. *Journal of Royal Statistical  
650 Society, Series B*, 61(3), 611–622.
- 651 Toker, D., & Sommer, F. T. (2019). Information integration in large brain networks. *PLoS Computational  
652 Biology*, 15(2), e1006807.
- 653 Tong, F., & Pratte, M. S. (2012). Decoding patterns of human brain activity. *Annual Review of Psychology*, 63,  
654 483–509.
- 655 Turk-Browne, N. B. (2013). Functional interactions as big data in the human brain. *Science*, 342, 580–584.
- 656 van der Maaten, L. J. P., & Hinton, G. E. (2008). Visualizing high-dimensional data using t-SNE. *Journal of  
657 Machine Learning Research*, 9, 2579–2605.
- 658 Vidaurre, D., Abeysuriya, R., Becker, R., Quinn, A. J., Alfaro-Almagro, F., Smith, S. M., & Woolrich, M. W.  
659 (2018). Discovering dynamic brain networks from big data in rest and task. *NeuroImage*, 180, 646–656.
- 660 Zar, J. H. (2010). *Biostatistical analysis*. Prentice-Hall/Pearson.
- 661 Zheng, M., Allard, A., Hagmann, P., & Serrano, M. A. (2019). Geometric renormalization unravels self-  
662 similarity of the multiscale human connectome. *arXiv*, 1904.11793.
- 663 Zou, Y., Donner, R. V., Marwan, N., Donges, J. F., & Kurths, J. (2019). Complex network approaches to  
664 nonlinear time series analysis. *Physics Reports*, 787, 1–97.